Available online at www.sciencedirect.com
SCIENCE DIRECT®
Vision Research 45 (2005) 3526–3534
Vision Research
www.elsevier.com/locate/visres

Polarimetric high-resolution confocal scanning laser ophthalmoscope

Juan M. Bueno, Brian Vohnsen *

Laboratorio de Óptica, Departamento de Física, Universidad de Murcia, Campus de Espinardo (Edificio C), 30071 Murcia, Spain

Received 2 June 2005; received in revised form 4 August 2005

Abstract

A polarimetric high-resolution confocal scanning laser ophthalmoscope has been developed. The system incorporates a fixed linear polarizer in the illumination path and a rotatory quarter-wave plate and another fixed linear polarizer in the registration path. Retinal areas that are smaller than those provided by commercial instruments can be imaged. Series of four fundus images for independent polarization states in the second pass were recorded for different eyes and retinal locations and the spatially resolved Stokes vectors calculated. From those images, the contrast across retinal blood vessels was maximized and the corresponding image was reconstructed. In terms of polarization, the analysis of small retinal areas might prove to be useful in the improvement of retinal imaging and the enhancement of structural details in the early diagnosis of ocular pathologies.

Keywords: Polarimetry; Retinal imaging; Confocal scanning laser ophthalmoscope; Contrast optimization

1. Introduction

In the last two decades, several polarimeters oriented to both basic research in physiological optics and clinical ophthalmological applications have been reported. The formers used rotating quarter-wave plates (QWP's) (Bueno & Campbell, 2002; Dreher, Reiter, & Weinred, 1992; van Blokland, 1985), pockel cells (Pelz et al., 1996) or liquid crystal modulators (Bueno, 2000; Bueno & Artal, 1999) to provide the Mueller matrix of the human eye. With this information, the polarization properties of the living eye or the in vitro retina, the cornea (Bueno & Jaronski, 2001; van Blokland & Verhelst, 1987) or the crystalline lens (Bueno & Campbell, 2003; klein Brink, 1991) can be obtained. Clinical instruments are much simpler in terms of polarimetry since they use linear incident light and a pair of polarization-sensitive detectors (usually named as parallel and crossed) (Hunter, Patel, & Guyton, 1999; Knighton & Huang, 2002). Moreover, these commercial setups are focused on the ocular (mainly retinal) birefringence for glaucoma diagnosis (Greenfield, Knighton, & Huang, 2000; Garway-Heath, Greaney, & Caprioli, 2002; Zhou & Weinreb, 2002) or for detection of foveal fixation (Hunter et al., 1999; Hunter, Shah, Sau, Nassif, & Guyton, 2003). They do not, however, take into account (or not totally) other ocular polarization properties such as depolarization, which can be very important in older eyes or in eyes suffering from some pathology (Burns, Elsner, Mellem-Kairala, & Simmons, 2003).

One of the authors previously compared the results in ocular retardation and azimuth obtained when considering the young human eye as a linear retarder and those calculated directly from the Mueller matrix (Bueno, 2002). Differences were small basically due to the low depolarization present in young eyes. When including older eyes errors increased (Bueno, 2004), which indicates that depolarization effects cannot always be neglected in ocular polarimetry. However, the use of linear polarizers do not inform completely on

* Corresponding author. Tel.: +349 6839 8315; fax: +349 6836 3528.
E-mail address: vohnsen@um.es (B. Vohnsen).

0042-6989/$ - see front matter © 2005 Elsevier Ltd. All rights reserved.
doi:10.1016/j.visres.2005.08.008

depolarization effects since the circular component cannot be calculated. This configuration might also erroneously identify completely polarized states as partially depolarized (Bueno, 2001a, 2002).

It is well-known that the measurement of the Mueller matrix of an optical system requires (at least) four independent polarization states in both the generator and the analyzer unit (AU) (see Chipman, 1995, chap. 22 for further information). Then, four polarization states are required in the AU to calculate the Stokes vector of a light beam. However, if one polarization property is much more important than the rest, the complete Mueller matrix is not required (Azzam & Bashara, 1992; Chipman, 1995, chap. 22) and the procedure can be simplified. Such an experimental system is known as an incomplete polarimeter (Chipman, 1995, chap. 22) or polariscope (Theocaris & Gdoutos, 1979) (linear polariscope when incorporating just linear polarizers). In this context, a polarimetric system composed of a fixed linear polarizer in the incoming pathway and an AU in the outgoing pathway has been recently reported in Bueno, Berrio, and Artal (2003). This AU is composed of a rotatory QWP and another fixed linear polarizer. With this configuration, the emerging Stokes vector can be calculated. From this vector, information on depolarization and birefringence can be obtained. This approach has been implemented in a double-pass setup (Bueno, 2004), in a Hartmann–Shack wavefront sensor (Bueno et al., 2003), and in a dual (double-pass and Hartmann–Shack) system (Bueno, Berrio, Ozolinsh, & Artal, 2004) to obtain ocular polarimetric information for different experimental conditions.

Early polarimeters used two stationary linear polarizers combined with two rotating QWP's. These were rotated in angular increments with different ratios (Azzam, 1978; Bernabeu & Gil, 1985; Hauge, 1978). The ratio between the angular speeds of both retarders produced a periodic intensity fluctuation and a Fourier analysis was required to compute the Mueller matrix. Later, some effort was made in calculating a set of four angles (at which the fast axis of the QWP must be oriented) that ensured an accurate calculation of the Stokes vector associated with a light beam (Ambirajan & Look, 1995). More recently, other authors reported that to optimize a complete Stokes polarimeter composed of a rotatable retarder and a fixed polarizer a retardation of 132° and a set of angles (−51.7°, −15.1°, 15.1°, 51.7°) are required (Sabatke et al., 2000). In the present work, we have used the set of angles (−45°, 0°, 30°, 60°) proposed in Ambirajan and Look (1995). This configuration has successfully been used in previous ocular polarimetric measurements (Bueno et al., 2003, 2004; Bueno & Campbell, 2003; Bueno & Jaronski, 2001).

The implementation of polarization techniques in imaging systems has been reported to improve contrast, reduce noise and provide useful information (Campbell, Bueno, & Hunter, 2002; Tyo, Rowe, Pugh, & Engheta, 1996;Tyo, 2000). In particular, polarimetry has been used to reduce noise and enhance confocal scanning laser ophthalmoscope (CSLO) images (Bueno & Campbell, 2002; Guthrie, Bueno, Kisilak, Hunter, & Campbell, 2004), as well as for enhancing retinal fundus features oriented to clinical diagnosis by either improving the contrast of subretinal structures or characterizing blood vessels (Burns et al., 2003; Weber, Cheney, Smithwick, & Elsner, 2004).

In the present work, we have incorporated the polarimetric device into a high-resolution CSLO. Series of four images associated with independent polarization states in the AU are registered. These images show small retinal areas (much smaller than those obtained with commercial polarimeters). From these images, the associated Stokes vector was reconstructed. Additionally, the collected images were also used to optimize the reconstructed intensity image in terms of blood vessel contrast and overall image appearance. This image was compared to the averaged intensity image and to the image that corresponds to the intensity of the Stokes vector.

2. Methods

2.1. Apparatus and experimental procedure

To perform imaging with polarization analysis we have modified our home-built CSLO (Vohnsen, Iglesias, & Artal, 2003) in such a manner that the polarization state in the detection path can be varied. In turn, the polarization state of the incident light is linear and kept fixed. The system is shown schematically in Fig. 1. For the illumination a near-IR laser diode (wavelength 785 nm) is used and the amount of power reaching the eye pupil is kept at or below 150 μW. This corresponds at most to ~25% of the permissible power in the small-source limit with continuous exposure (American National Standard Institute, 2000). Two galvanometric scanners (one of them resonant) allow 512×512 pixel-sized images to be recorded at a frame rate of ~15 Hz. The scanning range at the pupil of the incident light can be selected in the range of 1°–8°. Data are only collected in the forward direction of the raster scan, which corresponds to a sweep of individual pixels in less than 0.1 μs. The amount of light coupled back out of the eye is directed to a confocal pinhole whose diameter (200 μm) corresponds to ~30 μm on the retina taking into account the intrinsic system magnification. Before reaching the pinhole, however, a given polarization state is chosen with the AU. The confocally-filtered light is collected with a photomultiplier tube and a series of data (up to 16 subsequent frames for a given polarization state)

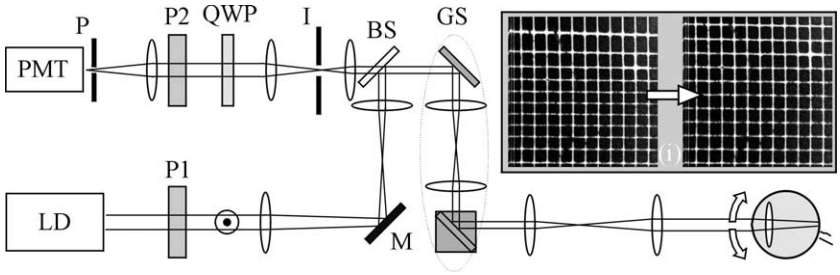

Fig. 1. Schematic of the confocal scanning laser ophthalmoscope used for high-resolution polarimetric studies. The individual components are: laser diode (LD), galvanometric scanners (GS) mounted in conjugate planes, photomultiplier tube (PMT), pinhole (P), beam-splitter (BS), adjustable iris (I), mirror (M), and various AR-coated achromatic lenses. A polarizer (P1) ensures linear polarization of the incident light beam, and the state of polarization of light leaving the eye is analyzed near the confocal pinhole by a quarter-wave plate (QWP) and a linear polarizer (P2). The inset (i) shows a calibration scan of a copper-on-glass mesh of 63.5 μm period before and after image linearization.

are stored with a LabView-controlled 20 MHz digital oscilloscope for subsequent visualization. Naturally, the harmonic motion of the resonant scanner distorts the recorded images and the images are therefore corrected with software before presentation (see inset in Fig. 1). Saccadic eye motion can have a more detrimental effect on the recorded images, but can be partially compensated (at least for motion between frames) by correlating and averaging subsequent frames. This also enhances image quality in terms of the signal-to-noise ratio. Typically, we correlate up to eight subsequent frames (covering a total time span of ~0.5 s). When more are included the final result is more prone to suffer from the ocular movements occurring within individual image frames.

Pupil decentration of the eye during experiments was minimized by use of an XYZ-mounted bite bar. A series of images corresponding to four independent polarization states in the AU were recorded. These were generated by orienting the fast axis of the retarder at four different orientations as described in detail elsewhere (Bueno et al., 2003) (see below). From these images, the pixel-by-pixel associated Stokes vector was computed. The first element of this vector is the actual spatially-resolved intensity (i.e., the image) reaching the AU and the rest contains information on the polarization state of the light emerging from the eye. Whereas, the former can only take on positive values, the range for the latter (once normalized) can vary in the range of −1 to 1. From the elements of the Stokes vectors, maps of different ocular polarization properties can be computed (Chipman, 1995, chap. 22).

2.2. Calculation of the Stokes vector and improvement of fundus images

Let $S_{OUT} = [S_0, S_1, S_2, S_3]^T$ denote the Stokes vector with intensity I, azimuth φ and ellipticity χ, associated with light reaching the AU. The registered set of images I_j ($j = 1, 2, 3, 4$) will be a result of

$$I_{PMT} = \begin{pmatrix} I_1 \\ I_2 \\ I_3 \\ I_4 \end{pmatrix} = M_{AU} \cdot \begin{pmatrix} I \\ I \cdot \cos(2\chi) \cdot \cos(2\varphi) \\ I \cdot \sin(2\chi) \cdot \cos(2\varphi) \\ I \cdot \sin(2\varphi) \end{pmatrix} = M_{AU} \cdot S_{OUT}, \quad (1)$$

where M_{AU} is the 4×4 auxiliary matrix defined in Bueno et al. (2003), associated with the independent polarization states produced by the AU. These states are generated by orienting the fast axis of the retarder at −45°, 0°, 30° and 60°, respectively. Alternatively, the Stokes vector can be computed as:

$$S_{OUT} = (M_{AU})^{-1} \cdot I_{PMT}, \quad (2)$$

where the intensity of S_{OUT} can be calculated as

$$S_0 = \sum_{k=1}^{4} A_{1k} \cdot I_k. \quad (3)$$

Here, A_{1k} represent the elements in the first row of the inverse of M_{AU}.

For a combination of a rotatory retarder and a linear polarizer it can be easily demonstrated that:

$$\sum_{k=1}^{4} A_{1k} = 2. \quad (4)$$

On the other hand, from the registered set of images I_k ($k = 1, 2, 3, 4$), alternative retinal images (I_{OUT}) can be constructed using four modified A_{1k} values ($\tilde{A}_{1k}$) while still adhering to the condition given in Eq. (4):

$$I_{OUT} = \sum_{k=1}^{4} \tilde{A}_{1k} \cdot I_k \quad (5)$$

and a positivity constraint $I_{OUT} > 0$ at any pixel. In Eq. (5), the coefficients represent a theoretical combination of four orientations of the fast axis of the retarder, and the retardation itself, which produce four independent polarization states (not necessarily experimentally realizable with the current AU). From Eq. (5), we can

determine the set of values that produce images with best quality in terms of a given criterion. In this work, we have sought to maximize the contrast across blood vessels.

One particular simple choice is $\tilde{A}_{1k} = 1/2$ for any k. In this case, the image obtained I_{OUT} will simply correspond to the numerical average of the four initial images (only weighted by their different intensity). However, such a solution, although beneficial in terms of signal-to-noise ratio for the final image, is not necessarily the solution that provides the best result in terms of blood vessel contrast. Thus, we have designed a numerical procedure where each original image is weighted by a factor $-2 \leqslant \tilde{A} \leqslant 2$ complying with Eq. (4) (i.e., that the sum of all coefficients add to two). In this scheme, the contrast of a given individual image or section (including a retinal blood vessel) is calculated and a weighted sum of all images complying with the best contrast improvement is sought. As contrast criteria, we have examined the applicability of both the visibility (Michelson contrast) C_{v}, where the signal at two selected image points with highest and lowest brightness respectively is compared, and the global rms-contrast C_{rms} (Peli, 1990) for an entire image. It should be stressed that the outcome when applying the former is not easily controlled since the result depends directly on the chosen set of points (thereby making it sensitive to unwanted pixel variations). On the opposite, the later provide more reliable improvements since the evaluation is global and therefore less disturbed by local pixel variations. The outcome of applying both methods will be discussed in the last section and be compared to both the original images, the averaged image (i.e., $\tilde{A}_{1k} = 1/2$ for all k), and the Stokes intensity image S_0 ($A_{11} = 1.0718$, $A_{12} = -0.3094$, $A_{13} = 0.6188$, and $A_{14} = 0.6188$).

3. Results

Fig. 2 shows sets of images collected using the polarimetric CSLO on the right eye of the two authors both with normal vision and ~35 years old. Each image is the average of eight subsequent frames, subtends 2° and corresponds to a different orientation of the QWP in the AU. Retinal locations (from the foveal centre) were also different: ~4° in the nasal direction for subject #1 (BV) and ~15° downwards for subject #2 (JMB).

For each subject, images can be seen to depend on the recorded polarization state. This is to be expected, as the eye changes the linear incoming light to an elliptical (partially polarized) state. Thus, the final quality of an image will depend strongly on the configuration of the AU. By visual inspection, it can be noted that the best image appearance is associated with orientation 0° for subject #1 and with 30° for subject #2. This observation is in fair agreement with the calculated rms-contrast of each image.

From these intensity images, the spatially resolved Stokes vectors were calculated in accord with Eq. (2). The outcome is depicted in Fig. 3 (in a transposed position). The vectors contain polarimetric information on the double-pass through the ocular media and the retinal reflection. It may be noted that in the case of subject #1 a capillary is clearly visible in only the first vector element whereas for subject #2 a capillary can be seen in all of the elements. Averaged and normalized Stokes vectors across the entire images were $[1.00, -0.85, 0.21, 0.09]^{\mathrm{T}}$ and $[1.00, 0.52, 0.07, -0.08]^{\mathrm{T}}$ for subject #1 and #2, respectively. These emergent Stokes vectors are depicted in Fig. 4 together with the incident one. Although changes in the polarization state are local, this (averaged) representation gives a global idea of changes suffered by light double-passing the eye and reflected off

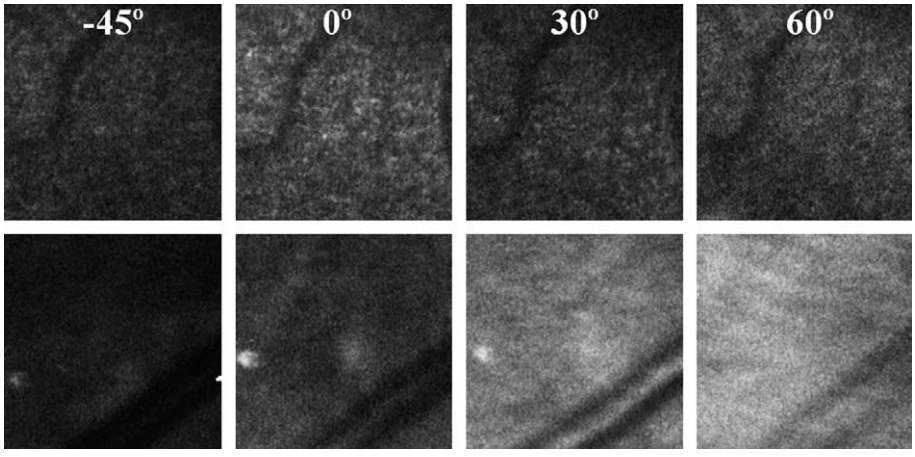

Fig. 2. CSLO images for subject #1 (upper panels) and #2 (bottom panels) corresponding to the four independent polarization states in the AU. Images subtend 2°. Retinal locations are given in the text. The global rms-contrast values were 0.057, 0.082, 0.064 and 0.072 for subject #1; and 0.047, 0.073, 0.097 and 0.109 for subject #2, for images corresponding to orientations −45°, 0°, 30° and 60°, respectively.

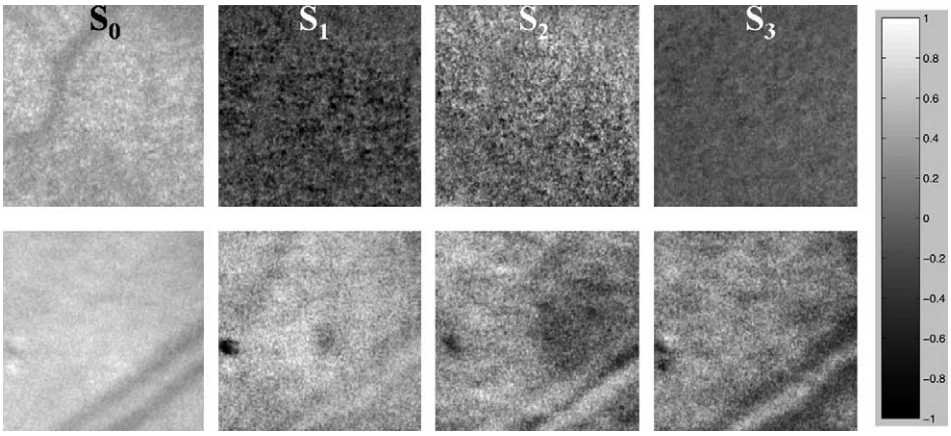

Fig. 3. Elements of the spatially-resolved Stokes vector for both subjects calculated from the images in Fig. 2. The gray-level code is shown at the right.

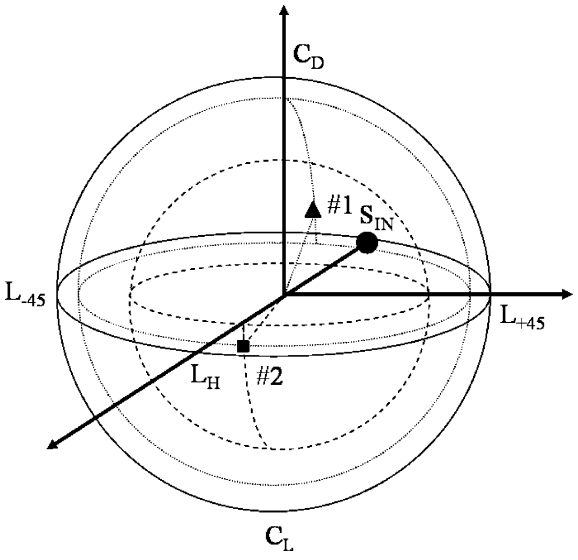

Fig. 4. Incident and (averaged) emergent Stokes vectors on the Poincaré sphere for subjects #1 and #2. Since the radius of the sphere represents the degree of polarization, emergent vectors are located within the (solid line) sphere of radius unity.

the retina. These are mainly due to two properties: depolarization and birefringence. The former turns a totally polarized incident state into a partially polarized one, i.e., the location of the outgoing state is inside the Poincaré sphere. The latter can be represented as a rotation about an axis passing through the center of the sphere. It may be noticed that the averaged state of polarization for the two cases studied is very different (nearly opposed on the Poincaré sphere) which presumably reflects a different (mostly) corneal contribution for the imaged eyes. In this context, it should be recalled that we are comparing two different eyes and two very different retinal locations, and to gain further insight in this respect would therefore require additional studies beyond the scope of the present paper. As an additional example, in Fig. 5, the degree of polarization (calculated directly from the Stokes vectors (Chipman, 1995, chap. 22)) is mapped for both subjects.

Although a blood vessel can be seen in the images of both subjects the Stokes representation (in particular S_0 when normalized between 0 and 1; see also Figs. 6A and E) does not guarantee an improved image quality and contrast as compared to the original set of images (Fig. 2). To look closer on this issue, we have evaluated the averaged image (I_{OUT} with all $\tilde{A}_{1k} = 1/2$). Moreover, combinations of the original image set that via Eq. (5) provide the globally highest and lowest rms-contrast,

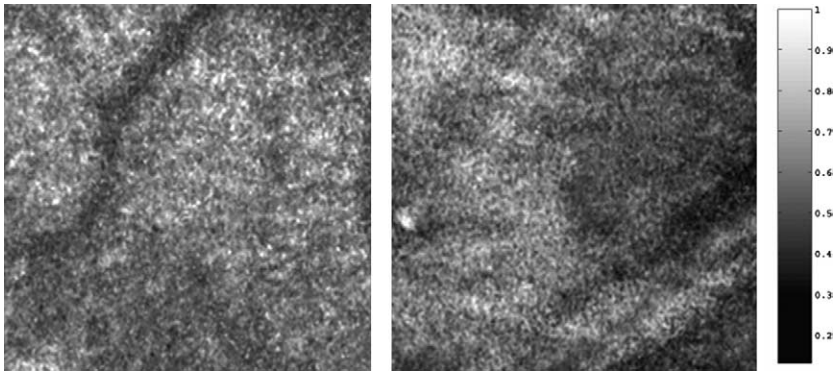

Fig. 5. Maps for the degree of polarization in subjects #1 and #2. These were calculated pixel by pixel from the vectors in Fig. 3.

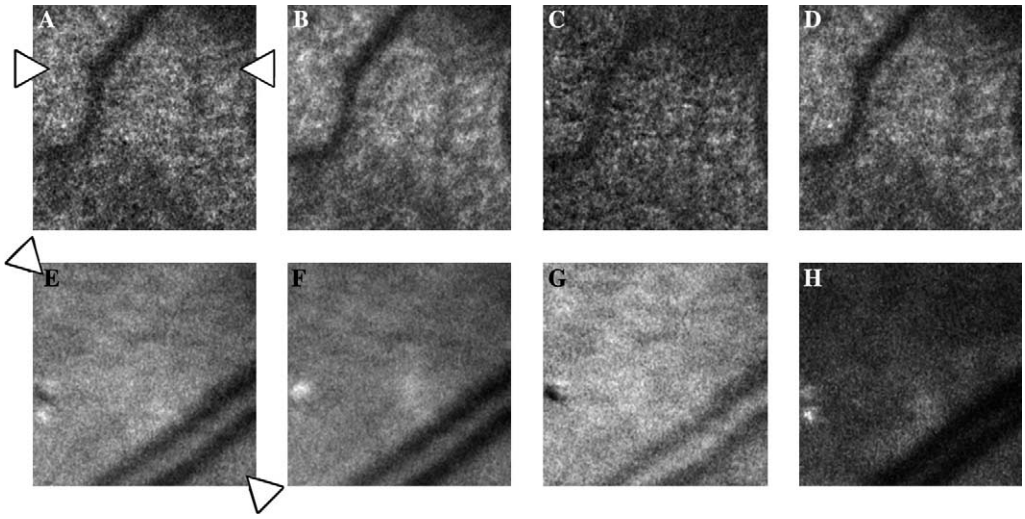

Fig. 6. (A and E) S_0 (normalized on 0 to 1); (B and F) averaged intensity; (C and G) image with maximized rms-contrast; (D and H) image with minimized rms-contrast.

Table 1
The rms-contrast C_{rms} of the images shown in Fig. 6[a]

Subject	S_0	Avr. I_{OUT}	High C_{rms}	Low C_{rms}
#1	0.09	0.10	0.22	0.09
#2	0.13	0.12	0.30	0.09

[a] Calculated globally on the entire images.

respectively, have been calculated. The outcome is shown in Fig. 6 for both subjects, and the optimized set of scaling parameters is: (C) $\tilde{A}_{11} = -2.0$; $\tilde{A}_{12} = 2.0$; $\tilde{A}_{13} = 1.9$; $\tilde{A}_{14} = 0.1$, (D) $\tilde{A}_{11} = +0.9$; $\tilde{A}_{12} = 0.0$; $\tilde{A}_{13} = 0.7$; $\tilde{A}_{14} = 0.4$; (G) $\tilde{A}_{11} = 0.0$; $\tilde{A}_{12} = -2.0$; $\tilde{A}_{13} = 2.0$; $\tilde{A}_{14} = 2.0$; and (H) $\tilde{A}_{11} = 1.7$; $\tilde{A}_{12} = 0.4$; $\tilde{A}_{13} = -0.1$; $\tilde{A}_{14} = 0.0$. The corresponding rms-contrast of each sub-image is given in Table 1. If instead of the rms-contrast the standard two-point visibility criterion is used in a small section, the outcome may either favor or hinder an easy detection (due to local pixel noise) of the blood vessel as shown in Fig. 7. To better quantify the contrast improvement obtained through the optimization, cross-sections across the blood vessel images of Fig. 6 (as indicated by arrow heads) have been made and their visibility have been calculated. The values found are given in Table 2.

Table 2
Standard (Michelson) contrast C_v across blood vessels from Fig. 6[a]

Subject	S_0	Avr. I_{OUT}	High C_{rms}	Low C_{rms}
#1	0.33	0.31	0.34	0.37
#2	0.43	0.49	0.27	0.67

[a] The contrast has been evaluated from the average of the two darkest points within and the average of the two brightest points on either side of the blood vessel. In all cases, the cross-section represents the average of five neighboring lines to reduce the influence of pixel-related noise.

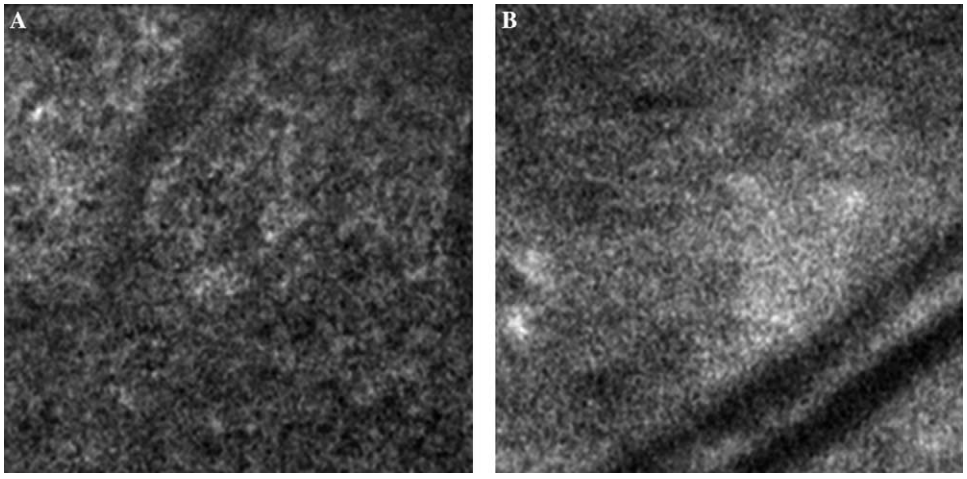

Fig. 7. Images with optimized standard (Michelson) contrast across the blood vessel for subject #1 (A) and #2 (B).

4. Discussion

We have calculated the Stokes parameter images for high-magnification retinal areas. Preliminary results in two subjects indicate that the eye noticeable changes the polarization state of the incident light. Thus, not only are there variations between the visibility of structures for the different Stokes elements (Fig. 3) presumably due to the combination of corneal and retinal birefringence and retinal depolarization. Rather, at these small scales changes are not uniform as can be observed from the non-uniformity of the individual elements of the vector. This can also be seen in the maps for the degree of polarization (Fig. 5). In the analyzed areas, values ranged from 0.13 to 0.92. Since the eyes correspond to young adult subjects, the main source for depolarization is supposedly the retina (Bueno, 2001b). At this point, the retinal structures responsible for the effect remain to be studied. Moreover, most of ocular birefringence is due to the cornea (Greenfield et al., 2000; Garway-Heath et al., 2002; Pelz et al., 1996; Zhou & Weinreb, 2002).

The implementation of polarimetric techniques into a CSLO has been reported for different purposes ranging from image enhancement (Bueno & Campbell, 2002; Guthrie et al., 2004) to the diagnosis of ocular pathologies (such as glaucoma) (Dreher et al., 1992; Greenfield et al., 2000; Garway-Heath et al., 2002; Pelz et al., 1996; Zhou & Weinreb, 2002). Commercial instruments provide very useful information on ocular birefringence but not on depolarization. If the real effects of depolarization are known, the error in the calculation of ocular retardation can be minimized (Bueno, 2004). It has recently been shown that depolarization is related to scatter (Bueno et al., 2004) and some retinal pathologies (Burns et al., 2003; Mellem-Kairala, Elsner, Weber, Simmons, & Burns, 2005). In addition, maps of depolarization allow to improve the contrast of retinal structures and they are useful in blood vessel visualization (Burns et al., 2003; Weber et al., 2004).

It may be noted that S_0 (normalized on 0 to 1) and the averaged intensity images are somewhat similar in appearance albeit the former appears to contain additional details that are less easily distinguished in the latter. This was to be expected as the average does not consider the actual polarization-resolved detection of the AU. In turn, the optimized rms-contrast images reveal either little selectivity to the blood vessel (Figs. 6C and G) or facilitate its detection (Figs. 6D and H). When the rms-contrast is largest the pixel-to-pixel variation of the final image is large and rapid variations are highlighted (this may be favorable to reveal tiny structures although random noise is also enhanced). The larger blood vessels, however, are best appreciated on a mostly uniform background as corresponding to a small global rms-contrast (ideally a binary-like signal with maximum outside and minimum inside of the vessel). This can also be appreciated from the tabulated contrast values that show that the best blood vessel visibility (Table 2) corresponds to the images optimized to provide the lowest rms-contrast (Table 1). This may appear counter-intuitive, but it is explained by the above argument. In turn, with the standard visibility optimization pixel noise makes the outcome less easy to predict than for the rms-contrast and the result may either deteriorate or be favorable for the image appearance (Fig. 7). From the results obtained, it is clear that a proper polarization analysis can significantly improve the visibility of a given structure like the blood vessels in the present case. Thus, for subject #1 the best improvement in contrast is approximately 10–20% when compared to either S_0 or the averaged intensity image and about 40–50% for subject #2 when making the same comparison. On the other hand, if no polarization analysis was performed the images would look similar to those of Fig. 2 where a standard contrast $C_v = 0.24$ can be found at the blood vessel for subject #1 (intensity image at 0°) and $C_v = 0.32$ in the case of subject #2 (intensity image at 30°). Thus, the polarimetric optimization process has led to an approximate doubling of the original blood vessel contrast as is apparent when comparing to Table 2 (last column).

5. Conclusions

In this work, we report on our newly developed high-resolution polarimetric CSLO and initial results obtained with the living human eye. The incident polarization state is kept fixed and four images of the retinal fundus associated with independent polarization states of the AU are recorded. The elements of the corresponding spatially resolved Stokes vector were computed from them and it was found that the image of S_0 provide images similar to or slightly better than the numerical average of all the intensity images. On the other hand, from the four recorded images, images with a higher contrast across a previously chosen blood vessel was looked for by numerically seeking more favorable combinations of the elements of the first row of the inverse of the matrix M_{AU}. In particular, we found that the best blood vessel visibility is obtained in images with a low rms-contrast and that the improvement can be on the order of up to ~50% as compared to that of S_0.

More than 10 years ago, polarization-sensitive optical coherence tomography (PS-OCT) technology was proposed (Hee, Huang, Swanson, & Fujimoto, 1992) as a powerful tool to explore the polarization properties of optical systems. This technique has been applied to different fields of research including the human eye (see reference, de Boer, 2002, for a general review). However, depolarization effects can not be calculated using

PS-OCT and only information on birefringence is provided. In this sense, a system providing information on depolarization like the one presented here could be of help in clinical diagnosis, in particular, if both approaches are combined in future studies.

Acknowledgments

The authors gratefully acknowledge valuable discussions with I. Iglesias and Prof. P. Artal in the early stage of this work. The research has been supported by the Ministerio de Educación y Ciencia, Spain (Grant FIS2004-02153 to P. Artal), the Fondo de Investigación Sanitaria (Grant FIS01/1463 to I. Iglesias and Grant red IM3 G03/185 to P. Artal), and Ramón y Cajal research contract (RYC2002-006337 to B.Vohnsen).

References

Ambirajan, A., & Look, D. C. Jr., (1995). Optimum angles for a polarimeter: Part I. *Optical Engineering, 34*, 1651–1655.

American National Standard Institute. (2000). *American National Standard for Safe Use of Lasers*, Laser Institute of America, Orlando.

Azzam, R. M. A. (1978). Photopolarimetric measurement of the Mueller matrix by Fourier analysis of a single detected signal. *Optics Letters, 2*, 148–150.

Azzam, R. M. A., & Bashara, N. M. (1992). *Ellipsometry and polarized light*. New York, NY: North-Holland.

Bernabeu, E., & Gil, J. J. (1985). An experimental device for the dynamic determination of Mueller matrices. *Journal of Optics (Paris), 16*, 139–141.

Bueno, J. M. (2000). Measurement of parameters of polarization in the living human eye using imaging polarimetry. *Vision Research, 40*, 3791–3799.

Bueno, J. M. (2001a). Indices of linear polarization for an optical system. *Journal of Optics A: Pure and Applied Optics, 3*, 470–476.

Bueno, J. M. (2001b). Depolarization effects in the human eye. *Vision Research, 41*, 2687–2696.

Bueno, J. M. (2002). Polarimetry in the human eye using an imaging linear polariscope. *Journal of Optics A: Pure and Applied Optics, 4*, 553–561.

Bueno, J. M. (2004). The influence of depolarization and corneal birefringence on ocular polarization. *Journal of Optics A: Pure and Applied Optics, 6*, S91–S99.

Bueno, J. M., & Artal, P. (1999). Double-pass imaging polarimetry in the human eye. *Optics Letters, 24*, 64–66.

Bueno, J. M., Berrio, E., & Artal, P. (2003). Aberro-polariscope for the human eye. *Optics Letters, 28*, 1209–1211.

Bueno, J. M., Berrio, E., Ozolinsh, M., & Artal, P. (2004). Degree of polarization as an objective method of estimating scattering. *Journal of the Optical Society of America A, 21*, 1316–1321.

Bueno, J. M., & Campbell, M. C. W. (2002). Confocal scanning laser ophthalmoscopy improvement by use of Mueller-matrix polarimetry. *Optics Letters, 27*, 830–832.

Bueno, J. M., & Campbell, M. C. W. (2003). Polarization properties for in vitro old human crystalline lens. *Ophthalmic and Physiological Optics, 23*, 109–118.

Bueno, J. M., & Jaronski, J. W. (2001). Spatially resolved polarization properties for in vitro corneas. *Ophthalmic and Physiological Optics, 21*, 384–392.

Burns, S. A., Elsner, A. E., Mellem-Kairala, M. B., & Simmons, R. B. (2003). Improved contrast of subretinal structures using polarization analysis. *Investigative Ophthalmology and Vision Science, 44*, 4061–4068.

Campbell, M. C. W., Bueno, J. M., & Hunter, J. J. (2002). Improvement of confocal scanning laser ophthamoloscope images using polarimetry. Annual meeting Abstract and Program Planner accessed at www.arvo.org. Association for the Research in Vision and Ophthalmoscopy. Abstract 953.

Chipman, R. A. (1995). Polarimetry. In M. Bass (Ed.) (2nd ed.). *Handbook of optics* (Vol. 2). New York: McGraw-Hill.

de Boer, J. F. (2002). Review of polarization sensitive optical coherence tomography and stokes vector determination. *Journal of Biomedical Optics, 7*, 359–371.

Dreher, A. W., Reiter, K., & Weinred, R. N. (1992). Spatially resolved birefringence of the retinal never fiber layer assessed with a retinal laser ellipsometer. *Applied Optics, 31*, 3730–3735.

Greenfield, D. S., Knighton, R. W., & Huang, X.-R. (2000). Effect of corneal polarization axis on assessment of retinal nerve fiber layer thickness by scanning laser polarimetry. *American Journal of Ophthalmology, 129*, 715–722.

Garway-Heath, D. F., Greaney, M. J., & Caprioli, J. (2002). Correction for the erroneous compensation of anterior segment birefringence with the scanning laser polarimeter for glaucoma diagnosis. *Investigative Ophthalmology and Vision Science, 43*, 1465–1474.

Guthrie, S. I., Bueno, J. M., Kisilak, M. L., Hunter, J. J., & Campbell, M. C. W. (2004). Polarimetry of the optic nerve head and lamina cribrosa, *Annual Meeting Abstract and Program Planner accessed* at www.arvo.org. Association for the Research in Vision and Ophthalmology. Abstract 2796.

Hauge, P. S. (1978). Mueller matrix ellipsometry with imperfect compensators. *Journal of the Optical Society of America, 68*, 1519–1528.

Hee, M. R., Huang, D., Swanson, E. A., & Fujimoto, J. G. (1992). Polarization-sensitive low-coherence reflectometer for birefringence characterization and ranging. *Journal of the Optical Society of America B, 9*, 903–908.

Hunter, D. G., Patel, S. N., & Guyton, D. L. (1999). Automated detection of foveal fixation by use of retinal birefringence scanning. *Applied Optics, 38*, 1273–1279.

Hunter, D. G., Shah, A. S., Sau, S., Nassif, D., & Guyton, D. L. (2003). Automated detection of ocular alignment retinal birefringence scanning. *Applied Optics, 42*, 3047–3053.

klein Brink, H. B. (1991). Birefringence of the human crystalline lens in vivo. *Journal of the Optical Society of America A, 8*, 1788–1793.

Knighton, R. W., & Huang, X.-R. (2002). Analytical methods for scanning laser polarimetry. *Optics Express, 10*, 1179–1189.

Mellem-Kairala, M. B., Elsner, A. E., Weber, A., Simmons, R. B., & Burns, S. A. (2005). Improved contrast of peripapillary hyperpigmentation using using polarization analysis. *Investigative Ophthalmology and Vision Science, 46*, 1099–1106.

Peli, E. (1990). Contrast in complex images. *Journal of the Optical Society of America A, 7*, 2032–2040.

Pelz, B. C. E., Weschenmoser, C., Goelz, S., Fischer, J. P., Burk, R. O. W., & Bille, J. F. (1996). In vivo measurement of the retinal birefringence with regard on corneal effects using an electro-optical ellipsometer. *Proceedings in SPIE, 2930*, 92–101.

Sabatke, D. S., Descour, M. R., Dereniak, E. L., Sweatt, W. C., Kemme, S. A., & Philips, G. S. (2000). Optimization of retardance for a complete Stokes polarimeter. *Optics Letters, 25*, 802–804.

Theocaris, P. S., & Gdoutos, E. E. (1979). *Matrix theory of photoelasticity*. Berlin: Springer-Verlag.

Tyo, J. S., Rowe, M. P., Pugh, E. N., Jr., & Engheta, N. (1996). Target detection in optically scattering media by polarization-difference imaging. *Applied Optics, 35*, 1855–1870.

Tyo, J. S. (2000). Enhancement of the point-spread function for imaging in scattering media by use of polarization-difference imaging. *Journal of the Optical Society of America A, 17*, 1–10.

van Blokland, G. J. (1985). Ellipsometry of the human retina in vivo: Preservation of polarization. *Journal of the Optical Society of America A, 2*, 72–75.

van Blokland, G. J., & Verhelst, S. C. (1987). Corneal polarization in the living human eye explained with a biaxial model. *Journal of the Optical Society of America A, 4*, 82–90.

Vohnsen, B., Iglesias, I., & Artal, P. (2003). Confocal scanning laser ophthalmoscope with adaptive optical wavefront correction. *Proceedings in SPIE, 4964*, 24–32.

Weber, A., Cheney, M. C., Smithwick, Q. Y. J., & Elsner, A. E. (2004). Polarimetric imaging and blood vessel quantification. *Optics Express, 12*, 5178–5190.

Zhou, Q., & Weinreb, R. N. (2002). Individualized compensation of anterior segment birefringence during scanning laser polarimetry. *Investigative Ophthalmology and Vision Science, 43*, 2221–2228.